

PAPER



Cite this: *Energy Environ. Sci.*,
2020, 13, 908

Received 11th December 2019,
Accepted 22nd January 2020

DOI: 10.1039/c9ee04007b

rsc.li/ees

A more stable lithium anode by mechanical constriction for solid state batteries†

Yibo Su,[‡] Luhan Ye,[‡] William Fitzhugh, Yichao Wang, Eva Gil-González, In Kim and Xin Li *

In solid state batteries, lithium dendrites form when the applied current density is higher than a critical value. The critical current density is often reported as 1–2 mA cm⁻² at an external pressure of around 10 MPa. In this work, a more advanced mechanical constriction technique is applied on a solid-state battery constructed with Li₁₀GeP₂S₁₂ (LGPS) as the electrolyte and a lithium metal/graphite composite as the anode, where the graphite layer was applied to prevent (electro-)chemical reactions between Li metal and LGPS, as well as a short-circuit upon the application of pressure. The decomposition pathway of LGPS at the anode interface is modified by this mechanical constriction design, and the growth of lithium dendrites is inhibited, leading to excellent rate and cycling performances. No short-circuit or lithium dendrite formation is observed for batteries cycled at a current density up to 10 mA cm⁻².

Broader context

Lithium metal anode is extremely attractive for lithium ion battery applications, which, unfortunately, is impeded by the notorious issue of lithium dendrite during battery cycling with serious safety concerns. All-solid-state batteries have long been considered as promising to prevent lithium dendrite penetration by ceramic solid electrolytes with obviously higher mechanical strength than liquid electrolytes. However, most previous studies found oppositely that the critical current density for solid batteries is often much lower, above which dendrites catastrophically grow. Here we demonstrate, for the first time, that an extremely high cycling rate up to 10 mA cm⁻² is enabled through a proper mechanical constriction design in solid batteries using the ceramic sulfide of Li₁₀GeP₂S₁₂ (LGPS) as the electrolyte and graphite protected Li metal as the electrode without lithium dendrite formation. Here materials-level mechanical constriction on the order of GPa is technically implemented by an external pressure on battery cells on the order of MPa, the chemically inert graphite interface and a right procedure for battery assembly. Such constriction modulates the reduction decomposition of LGPS at several interfaces through different kinetically-limited pathways with changing rates, which provides a new design strategy for all-solid-state lithium metal batteries with high-rate and long-term cycling capabilities.

Introduction

Solid state battery is one of the most promising candidates for next-generation batteries because of intrinsic safety advantages and the potential for a dendrite-free Li metal anode.^{1–4} Amongst different solid-state electrolytes, ceramic-sulfide solid electrolytes such as Li₁₀GeP₂S₁₂ (LGPS) and Li_{9.54}Si_{1.74}P_{1.44}S_{11.7}Cl_{0.3} (LSPS) have attracted significant attention due to the high ionic conductivities of 12–25 mS cm⁻¹.^{5–7}

However, these sulfide electrolytes often form unstable interfaces with Li metal.⁸ Assuming that the interface between the sulfide electrolyte and lithium metal has negligible charge density, the voltage at the contacting electrolyte will be 0 V

versus the lithium metal. At this interface, the electrochemical and chemical instabilities of the interface are equivalent, as the contacting electrolyte is always at 0 V *versus* the Li metal. Additionally, many studies have revealed the electrochemical instability of bulk LGPS and LSPS at low voltage.^{9,10} In particular, LGPS is expected to electrochemically reduce at voltages below 1.7 V.^{7,11} This process leads to the degradation of battery performance.¹² Previous studies have suggested that mechanical constriction can interplay with electrochemical stability to expand the voltage window of solid electrolytes.^{7,13–15} For LGPS and LSPS, the low voltage window can be expanded from approximately 1.7 V to 0.7 V *versus* lithium metal, enabling Li₄Ti₅O₁₂ as the anode. However, direct contact of LGPS or LSPS with the lithium metal anode for battery operation remains a challenge, and most previous studies used Li–In alloys as the anode instead.^{16–18}

Another problem for solid state batteries is the formation of Li dendrites when the current density is increased.^{19,20} The threshold current density for Li dendrite formation is defined

John A. Paulson School of Engineering and Applied Sciences, Harvard University, Cambridge, MA 02138, USA. E-mail: lixin@seas.harvard.edu

† Electronic supplementary information (ESI) available. See DOI: 10.1039/c9ee04007b

‡ Equal contribution.

as the critical current density,²¹ which largely depends on the type of electrolyte and the testing conditions. For $\text{Li}_7\text{La}_3\text{Zr}_2\text{O}_{12}$, the critical current density is as low as 0.6 mA cm^{-2} .²² When the current density is higher than the critical current density, voids form and accumulate on the Li–electrolyte interface during battery cycling,²⁰ which leads to a continuous increase of local current density until the threshold for dendrite formation, followed by a short circuit. However, it was found that pressure can effectively inhibit this process by reducing the voids. In a symmetric solid state battery using lithium metal to sandwich $\text{Li}_6\text{PS}_5\text{Cl}$ sulfide electrolyte on both sides for a $\text{Li}/\text{Li}_6\text{PS}_5\text{Cl}/\text{Li}$ battery construction, the critical current density can be increased from 0.2 to 1 mA cm^{-2} when the external pressure during the battery test increases from 3 MPa to 7 MPa .²⁰ Note that compared with LGPS or LSPS, Li–P–S based electrolytes without Ge or Si element at some chemical compositions were found to give more stable battery performances in direct contact with the lithium metal anode.^{5,23,24}

Here, we show that an advanced mechanical constriction method can improve the stability of the lithium metal anode in solid state batteries with LGPS as the electrolyte. More importantly, we demonstrate that there is no Li dendrite formation and penetration even after a high rate test at 10 mA cm^{-2} in a symmetric battery. The mechanical constriction method is technically realized through applying an external pressure of 100 MPa to 250 MPa on the battery system through a volume constricted battery cell, where the Li metal anode is covered by a graphite film (G) that separates the LGPS electrolyte layer in the battery assembly to prevent the interface chemical reaction. Furthermore, such constriction also enforces a close contact on the interfaces between electrolyte particles, as well as between the electrolyte layer and the Li/G anode, where a materials-level mechanical constriction on the order of GPa is

realized on the otherwise exposed and thus unconstrained particle surface, to prevent the interface electrochemical reaction in battery tests. At the optimal Li/G capacity ratio, our method leads to excellent cyclic performances in both Li/G –LGPS– G/Li symmetric batteries and Li/G –LGPS– LiCoO_2 (LiNbO_3 coated) all-solid-state batteries. We show that upon cycling, the Li/G anode transforms from two layers into one integrated composite layer. Comparison between Density Functional Theory (DFT) computation and X-ray Photoelectron Spectroscopy (XPS) analysis yields the first ever direct observation of mechanical constriction controlling the decomposition reaction of LGPS. Moreover, the degree of decomposition is seen to become significantly suppressed under optimum constriction conditions.

Design of the Li/graphite anode

We first investigate the chemical stability between LGPS and (lithiated) graphite through the high temperature treatment of their mixtures at $500 \text{ }^\circ\text{C}$ for 36 hours inside an argon filled glovebox for an accelerated reaction.¹³ XRD measurements are performed on different mixtures before and after heat treatment, as shown in Fig. 1(A–C). Severe decomposition of LGPS in contact with lithium was observed accompanied by Li_2S , GeS_2 and Li_5GeP_3 formation (Fig. 1A). In contrast, no peak change occurs for the mixture of LGPS and graphite after heating, as shown in Fig. 1(B), demonstrating that graphite is chemically stable with LGPS. After heating the mixture of Li and graphite powders, lithiated graphite is synthesized (Fig. S1, ESI†). When the lithiated graphite is further mixed with LGPS, it is demonstrated to be largely chemically stable in Fig. 1(C), with only a slight intensity change for the 26° peak.

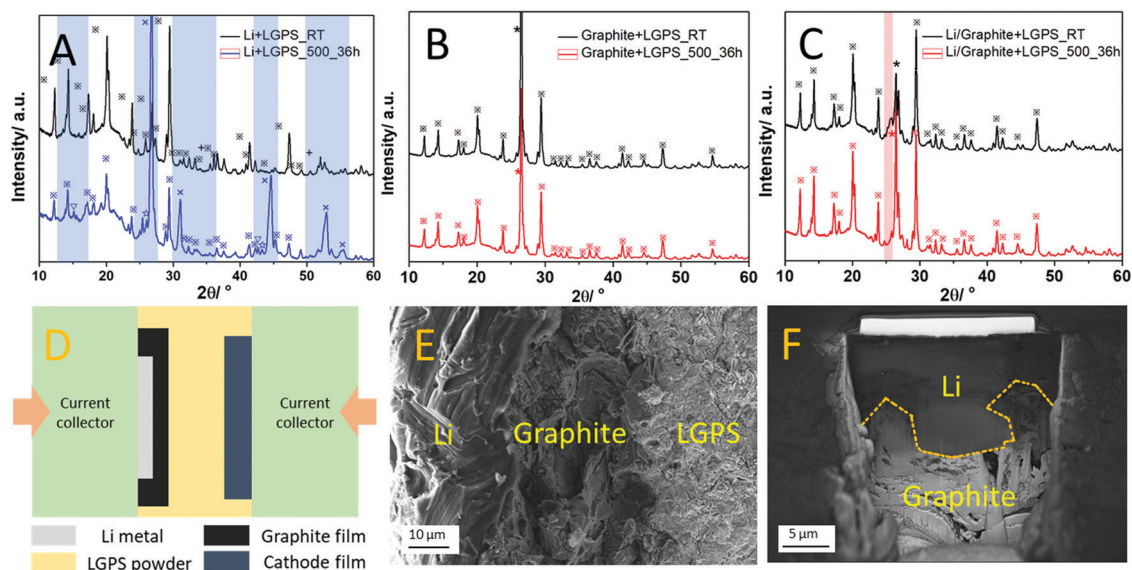


Fig. 1 (A–C) XRD of different powder mixtures before and after heat treatment at $500 \text{ }^\circ\text{C}$ for 36 hours ((A) Li + LGPS; (B) graphite + LGPS; (C) lithiated graphite + LGPS). The symbols and corresponding phases are: \otimes LGPS; $+$ Li; $*$ graphite; \times Li_2S ; ∇ GeS_2 ; \star Li_5GeP_3 . (D) The structure of the Li/graphite anode in the LGPS based all-solid-state battery; (E) SEM image of the cross section of the Li/graphite anode; and (F) FIB-SEM of the interface of Li and graphite.

The Li/graphite anode is thus designed as illustrated in Fig. 1(D). The protective graphite film was made by mixing graphite powder with PTFE and then covering onto the lithium metal. The three layers of the Li/graphite anode film, the electrolyte layer and the cathode film are stacked together sequentially, followed by mechanical pressing. The pressure was maintained at 100–250 MPa during the battery test. Such pressure helps obtain a good contact between the electrode and the electrolyte based on the conventional wisdom in this field,^{20,25–28} but, more importantly, it serves as a mechanical constriction for improved electrochemical stability of the solid electrolyte, as will be discussed later when XPS is compared with DFT.^{7,14,15} Scanning electron microscopy (SEM) shows that the graphite particles transform into a dense layer under such high pressure (Fig. S2, ESI†). The as-prepared anode before the battery test can be directly observed *via* SEM and focused ion

beam (FIB)-SEM in Fig. 1(E and F). The three layers of Li, graphite and LGPS are clear with close interface contact.

Cyclic and rate performance of the Li/graphite anode

Li/graphite anode in symmetric batteries

The electrochemical stability and rate capability of the Li/graphite (Li/G) anode are tested with an anode-LGPS-anode symmetric battery design under 100 MPa external pressure. The comparison of cyclic performance between the Li/G-LGPS-G/Li and Li-LGPS-Li batteries is shown in Fig. 2(A). The Li symmetric battery works only for 10 hours at a current density of 0.25 mA cm^{-2} before failure, while the Li/G symmetric battery is still running after 500 hours of cycling with the overpotential increasing slowly to

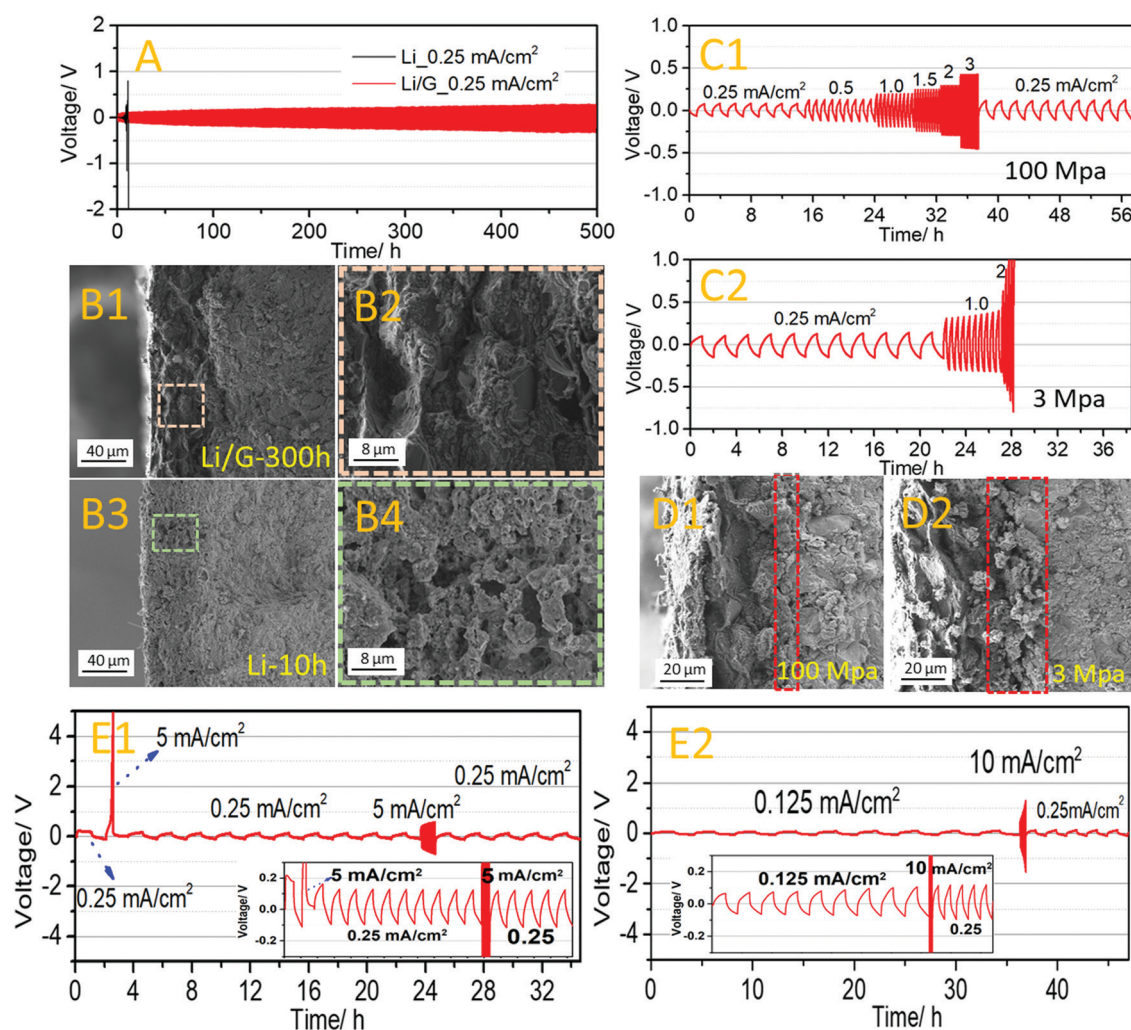


Fig. 2 (A) The comparison of cyclic performance between the Li/G-LGPS-G/Li and Li-LGPS-Li symmetric batteries; (B) the SEM images of the symmetric batteries after cycling. The Li/G-LGPS-G/Li symmetric battery after 300 hours' cycling (B1 and 2) and the Li-LGPS-Li symmetric battery after 10 hours' cycling (B3 and 4); (C) the rate performance of Li/G-LGPS-G/Li symmetric batteries under different pressures. (D) The SEM images of Li/G-LGPS-G/Li symmetric batteries under different pressures. (E) The ultra-high rate performance up to 10 mA cm^{-2} of Li/G-LGPS-G/Li symmetric batteries. The pressure applied in (E) is 250 MPa. The insets are the cycling profiles plotted in the range of -0.3 V to 0.3 V , showing that there is no obvious change of the overpotential after the high rate cycling. More voltage profile enlargements are shown in Fig. S6 (ESI†).

0.28 V. The stable cyclic performance is repeatable, as shown in Fig. S3 (ESI[†]) from another battery with a slower overpotential increase from 0.13 V to 0.19 V after 300 hours' cycling, indicating that such a slight overpotential change varies with the battery assembly. SEM shows that the Li/graphite anode transforms from two layers to one integrated composite layer without notable change of the total thickness after long-term cycling (Fig. S4, ESI[†]). The SEM images of the Li/G anode after 300 hours' cycling in a symmetric battery are compared with the Li anode after 10 hours' cycling in Fig. 2(B). The Li/G anode maintains a dense layer of lithium/graphite composite after the long-term cycling (Fig. 2B1 and B2). In comparison, there appear countless pores in the Li anode after 10 hours of testing, which are most probably induced by the severe decomposition reaction of LGPS with Li metal. The pores are harmful to both the ionic and electronic conductivities, which might be responsible for the sharp voltage increase when the Li symmetric battery fails at 10 hours. Note that the Li/G composite after cycling shows a black color (Fig. S4C, ESI[†]), indicating no obvious Li staging in graphite at or beyond LiC₁₈.²⁹

We also compare the rate performance of the Li/G symmetric battery under different external pressures of 100 MPa or 3 MPa as shown in Fig. 2(C). The same charging and discharging capacities were set for different current densities by changing the working time per cycle. At 100 MPa the Li/G symmetric battery can cycle stably from 0.25 mA cm⁻² up to 3 mA cm⁻² with an overpotential increase from 0.1 V to 0.4 V and can then cycle back normally to 0.25 mA cm⁻² (Fig. 2C1) with a very slight increase of the overpotential, while at 3 MPa the battery fails during the test at 2 mA cm⁻² (Fig. 2C2). Note that at the same current density, the overpotential at 100 MPa is only around 63% of that under 3 MPa. The shape of the potential-time curve is related to the diffusivities of Li⁺ ions. The diffusivity of lithium ions in graphite (10⁻⁹ cm² s⁻¹)³⁰ is much smaller than that in LGPS (10⁻⁴ cm² s⁻¹).³¹ The growth of polarization from the graphite layer makes the curve shape more like a zigzag curve.³² The SEM images of the Li/G-LGPS interface after the rate test up to 2 mA cm⁻² show close interface contact at 100 MPa (Fig. 2D1), while cracks and voids are observed after the test at 3 MPa (Fig. 2D2). Thus, the external pressure first plays the role of maintaining the close interface contact during the battery test, contributing to the better rate performance.

To further understand the influence of the Li/G composite formed by battery cycling on its high rate performance, a battery test has been designed like Fig. 2(E1). Here, a higher external pressure of 250 MPa was kept during the test. It starts at 0.25 mA cm⁻² for 1 cycle and then directly goes to 5 mA cm⁻² charge, which shows a sharply increased voltage that leads to the safety stop. We then restarted the battery instantly, running at 0.25 mA cm⁻² again for ten cycles followed by 5 mA cm⁻² for the next ten. This time the battery runs normally at 5 mA cm⁻² with an average overpotential of 0.6 V, and it can still go back to cycle at 0.25 mA cm⁻² without an obvious overpotential increase. At a fixed current, the initial voltage surge at 5 mA cm⁻² indicates a resistance jump, which is most probably related to the fact that Li and graphite are two layers as assembled, and hence there is

not sufficient Li in graphite to support such a high current density. However, after 20 hours' cycling at 0.25 mA cm⁻², Li/G is on the track of turning into a composite, as shown in Fig. 2(B) and Fig. S4 (ESI[†]), with much more Li storage to support the high rate cycling test. A long high-rate cycling performance was realized by charging the symmetric battery at 0.25 mA cm⁻² and discharging at 5 mA cm⁻² (Fig. S5, ESI[†]). Li in graphite is replenished by the slow charge, which prevents the kinetic limit due to the inefficient Li storage and the increase of the overpotential with high rate cycling.

Based on the above understanding, we further lowered the current density for the initial cycles to 0.125 mA cm⁻² and cycled with the same capacity of 0.25 mA h cm⁻² for a more homogeneous Li distribution and storage in the Li/G composite for improved lithium transfer kinetics. As shown in Fig. 2(E2), the battery can cycle at a current density of 10 mA cm⁻² and cycle normally when the current density was set back to 0.25 mA cm⁻². Note that there is no obvious overpotential increase at the same low current rate before and after the high rate test, as shown in the insets of Fig. 2(E) and Fig. S6 (ESI[†]), where the SEM of the Li/G anode of this battery also shows a clear formation of the Li/G composite without obvious Li dendrites observed on the interface.

Li/graphite anode in all-solid-state batteries

The Li/G anode is applied to a Li/G-LGPS-LiCoO₂ (LCO) (LiNbO₃ coated) construction of solid-state batteries. It is notable that various capacity ratios of Li to graphite lead to different initial charging/discharging curves, initial Coulombic efficiencies (iCE) and open circuit voltages (OCV) as shown in Fig. 3(A-C). When there is only graphite as the anode, the iCE is only 32.6% with an OCV of 0.16 V. The poor iCE is due to the Li consumption in the graphite anode, which is not necessarily due to intercalation, but may also be consumed by the capacitor effect and defects on the surface of graphite particles. The very low OCV is due to the fact that the voltage of graphite without Li intercalation is higher than 2 V, which is close to the OCV of LCO. In addition, there is no chemical reaction between graphite and LGPS, so graphite can keep its original high voltage. However, there is no extra lithium source replenishing the full battery, giving a poor cycling performance of the battery with pure graphite as the anode (Fig. S7, ESI[†]). When the Li/G capacity ratio increases, both the iCE and OCV rise until a Li/G ratio of 2.5:1, where the iCE is 91.4% and the OCV is around 2.0 V, which shows the best cycling performance among the different ratios (Fig. S7, ESI[†]). A further increase of the Li/G ratio gives a higher OCV while the iCE and the cycling capacity drop. This could be due to the reaction between Li and LGPS when less graphite is applied. When only using Li as the anode, the iCE is only 66.0% despite a high OCV of 2.4 V, while the battery cannot cycle. From the cycling performance, OCV and iCE of batteries with different Li/G ratios, we suggest that Li metal acts as a Li ion source in the composite anode, while graphite is largely a protection layer to prevent the interface reaction between LGPS and Li. More graphite, however, will consume more lithium. The competition between those two factors of protection and consumption gives

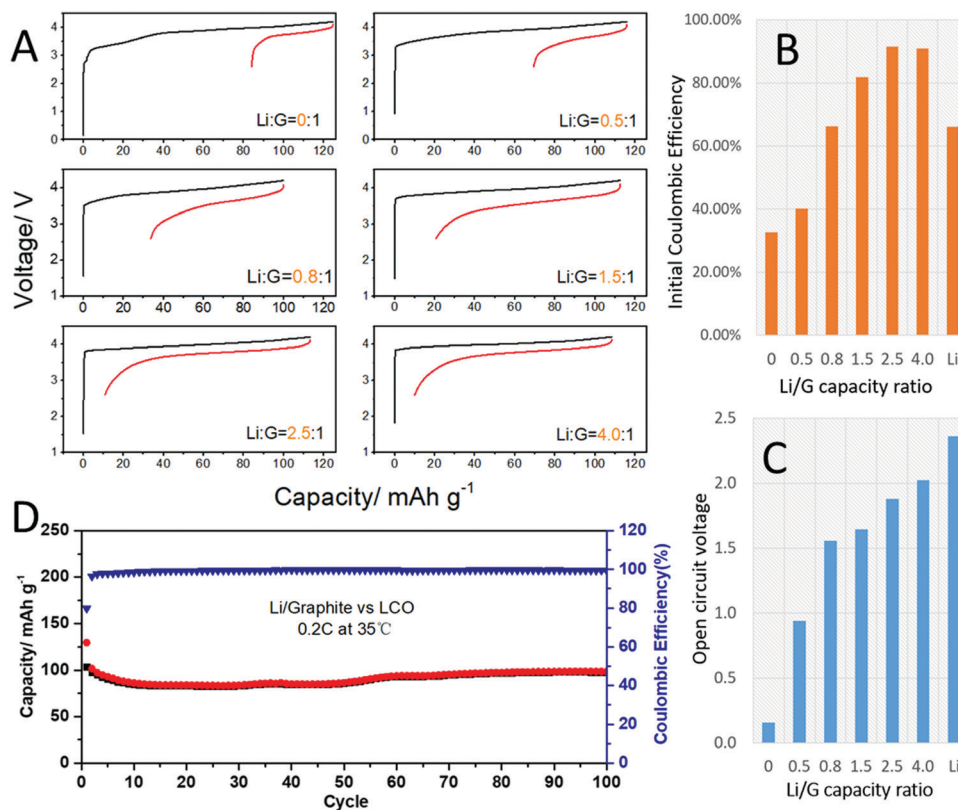


Fig. 3 (A) The comparison of the initial charge/discharge curves, (B) the initial Coulombic efficiencies and (C) the open circuit voltages after 1 hour rest, for different capacity ratios of Li to graphite in the Li/G-LGPS-LCO (LiNbO₃ coated) system. The Li/G capacity ratio of 0, 0.5, 0.8, 1.5, 2.5 and 4 can be translated into a Li/G thickness ratio of around 0, 0.3, 0.4, 0.8, 1.3, and 2.1 respectively, where the weight of Li metal remains the same at ~1 mg and the weight of graphite varies. Without a specific explanation, the Li/graphite thickness ratio is 1.0–1.3 by default in this work. (D) Cyclic performance of the Li/G-LGPS-LCO (LiNbO₃ coated) battery.

an optimal Li/G ratio of 2.5 : 1 (thickness ratio = 1.3 : 1). With the optimal Li/G anode, a stable cyclic performance is realized with the capacity stabilized at around 100 mA h g⁻¹ (based on LCO) as shown in Fig. 3(D). The corresponding voltage profiles are shown in Fig. S7A (ESI[†]). In contrast, the poor cyclic performance using Li as the anode is shown in Fig. S7B (ESI[†]).

The stability mechanism of LGPS at low voltages under mechanical constriction

The platform we invented here that uses the Li/graphite composite to enable high external pressure in battery operation gives us the opportunity to directly test our unique physical picture that both the voltage stability window and decomposition pathway can be modulated by mechanical constriction on the materials level. This investigation will also help elucidate the fundamental details about how the Li/G anode works well with LGPS under external pressure. We first perform DFT simulations of the LGPS decomposition pathways in the low voltage range of 0.0–2.2 V *versus* lithium metal. Following previous works,^{7,14,15} the mechanical constriction on the materials level is parameterized by an effective bulk modulus (K_{eff}) of

the system. Based on the value of this modulus, the system can range from isobaric ($K_{\text{eff}} = 0$) to isovolumetric ($K_{\text{eff}} = \infty$). The expected values of K_{eff} in real battery systems are on the order of 15 GPa.^{7,14,15} In the following, these simulation results are used to interpret XPS results of the valence changes of Ge and P from LGPS in the solid state batteries after CV, rate and cycling tests.

As shown in Fig. 4(A), the decomposition capacity of LGPS is lower at high effective moduli, indicating that the decomposition of LGPS at low voltage is largely inhibited by mechanical constriction. The predicted decomposition products and fraction number are listed in Fig. 4(B) and Table S1 (ESI[†]), respectively. At $K_{\text{eff}} = 0$ GPa (*i.e.* no applied mechanical constraint/isobaric), the reduction products approach the lithium binaries Li₂S, Li₃P, and Li_{1.5}Ge₄ as the voltage approaches zero. This is consistent with previous computational predictions.³³ However, after mechanical constriction is applied and the effective modulus is set at 15 GPa, the formation of Ge element, Li_xP_y and Li_xGe_y are suppressed, while compounds like P_xGe_y, GeS, and P₂S are emergent. This is also in agreement with the fact that P_xGe_y is known to be a high pressure phase.³⁴ The voltage profiles and reduction products at different K_{eff} shown in Fig. 4 indicate that the decomposition of LGPS follows different reduction pathways at low voltage after the application of mechanical constriction.

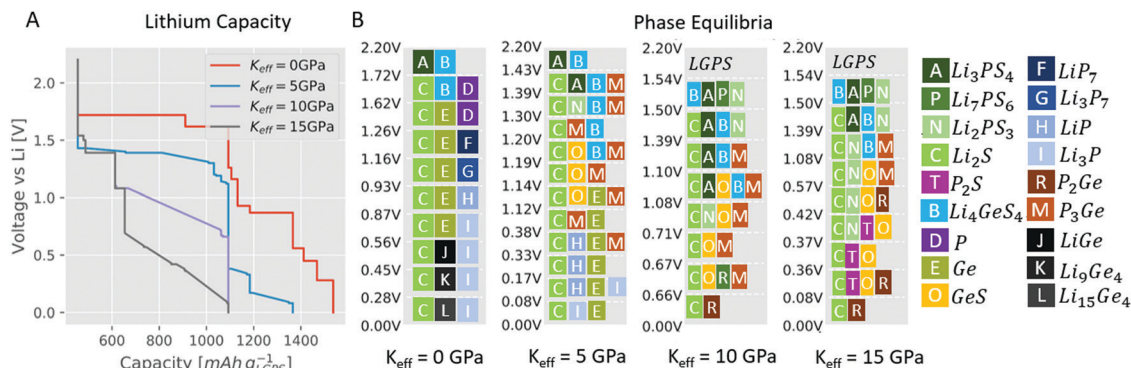


Fig. 4 (A) Voltage profiles of LGPS decomposition at different effective moduli (K_{eff}). (B) Reduction reaction pathways corresponding to different K_{eff} and the products in different phase equilibria within each voltage range. All decomposition products here are the ground state phases within each voltage range. The exact decomposition reactions are listed in Table S1 (ESI[†]).

It is worth noting that while the applied pressure and the effective modulus (K_{eff}) are both measured in units of pressure, they are independent. The effective modulus represents the intrinsic bulk modulus of the electrolyte added in parallel with the finite rigidity of the battery system.^{7,14,15} Accordingly, K_{eff} measures the mechanical constriction that can be realized on the materials level in any single particle,^{14,35} while the external pressure applied on the operation of a solid state battery is necessary to enforce the effectiveness of such constriction on the interface between particles or between the electrode and electrolyte layers.¹⁴ This is because an exposed surface is the most vulnerable to chemical and electrochemical decomposition, while close interface contact enforced by external pressure will minimize such a surface. Thus, even though the applied pressure is only on the order of 100 MPa, the effective bulk modulus is expected to be much larger. In fact, based on ref. 14, close packed LGPS particles should experience a K_{eff} of approximately 15 GPa. The applied pressure of 100–250 MPa is an effective tool for obtaining this close packed structure. In short, the applied pressure minimizes gaps in the bulk electrolyte, allowing for the effective modulus that represents the mechanical constriction on the materials level to approach its ideal value of *circa* 15 GPa.

The XPS results of LGPS that was either in a direct contact with lithium or lithium–graphite anode, or in the region away from that contacting interface, during battery cycling are provided in Fig. 5. These measurements of valence change can be well understood in light of the phase predictions of Fig. 4(B). LGPS in the separator region far from the anode interface shows Ge and P peaks identical to the pristine LGPS (Fig. 5A). This is consistent with previous literatures,^{8,36,37} which gives the Ge⁴⁺ and PS₄³⁻ reference valence states for the following comparison.

We first investigate the function of the Li/G composite in comparison with pure lithium metal at a slow rate of 0.25 mA cm⁻² under 100 MPa external pressure (Fig. 5B and C). With pure lithium metal (Fig. 5C) the reduction of both Ge and P is significant on the Li–LGPS interface, showing the formation of a Li_xGe_y alloy,³⁷ elemental Ge,³⁸ and Li₃P.^{8,39,40} Note that the Ge valence in Li_xGe_y and P valence in Li₃P are negative or below zero valence, consistent with the Bader charge analysis from DFT simulations (Fig. S8, ESI[†]). In contrast, with the Li/G anode

the reduction is inhibited on the Li/G–LGPS interface, with both the Ge and P valences remaining above zero in the decomposed compounds (Fig. 5(B)). The Li and LGPS interface is chemically unstable, leading to decompositions⁸ that include the observed compounds in Fig. 5(C). These decompositions are also consistent with the predicted ones in Fig. 4(B) at K_{eff} at 0 GPa. Further electrochemical cycling of such a chemically decomposed interface will cause the decomposed volume fraction to grow, ultimately consuming all of the LGPS. On the contrary, the graphite layer in the Li/G anode prevents the chemical interface reaction between LGPS and Li, while under the proper mechanical constriction the electrochemical decomposition seems to go through a pathway of high $K_{\text{eff}} \geq 10$ GPa in Fig. 4(B), where GeS, P₃Ge, and P₂S match the observed valences from XPS in Fig. 5(B).

When the cycle rate is increased to 2 mA cm⁻² and 10 mA cm⁻², the observed decompositions on the Li/G–LGPS interface under external pressures in Fig. 5(D) and (E) change to a metastable pathway that is different from the low rate one at 0.25 mA cm⁻² in Fig. 5(B). This implies that while Fig. 5(B) agrees with the thermodynamics predicted in Fig. 4, at high current densities the decomposition becomes kinetically dominated. Moreover, it is concluded that the Li/Ge alloy formation seen in Fig. 5(D) and (E) is the kinetically preferred phase in place of the reduced P. Specifically, Ge⁰ and Li_xGe_y, together with Li₃PS₄ and Li₇PS₆ are the most possible decompositions based on the valences from XPS. Note that at an external pressure of 3 MPa and hence reduced K_{eff} on the interfaces, both Ge and P reductions are observed even at a high rate of 2 mA cm⁻² (Fig. 5F), consistent with the general trend predicted at low K_{eff} in Fig. 4(B). However, the P reduction might still be kinetical rate-limited, as the most reduced state of Li₃P, as predicted in Fig. 4(B) at $K_{\text{eff}} = 0$ GPa and observed in Fig. 5(C) from the interface chemical reaction, was not observed.

Following the discussion in ref. 41 these two competing reactions with thermodynamic and kinetic preferences, respectively, can be understood by considering a current dependent overpotential ($\eta'(i)$) for each of these two competing reactions ($\eta \rightarrow \eta + \eta'(i)$). This η' term would arise from kinetic effects such as ohmic losses, *etc.* When the current is small ($i \approx 0$), η' disappears, and thus the thermodynamic overpotential (η) dominates and favors the ground

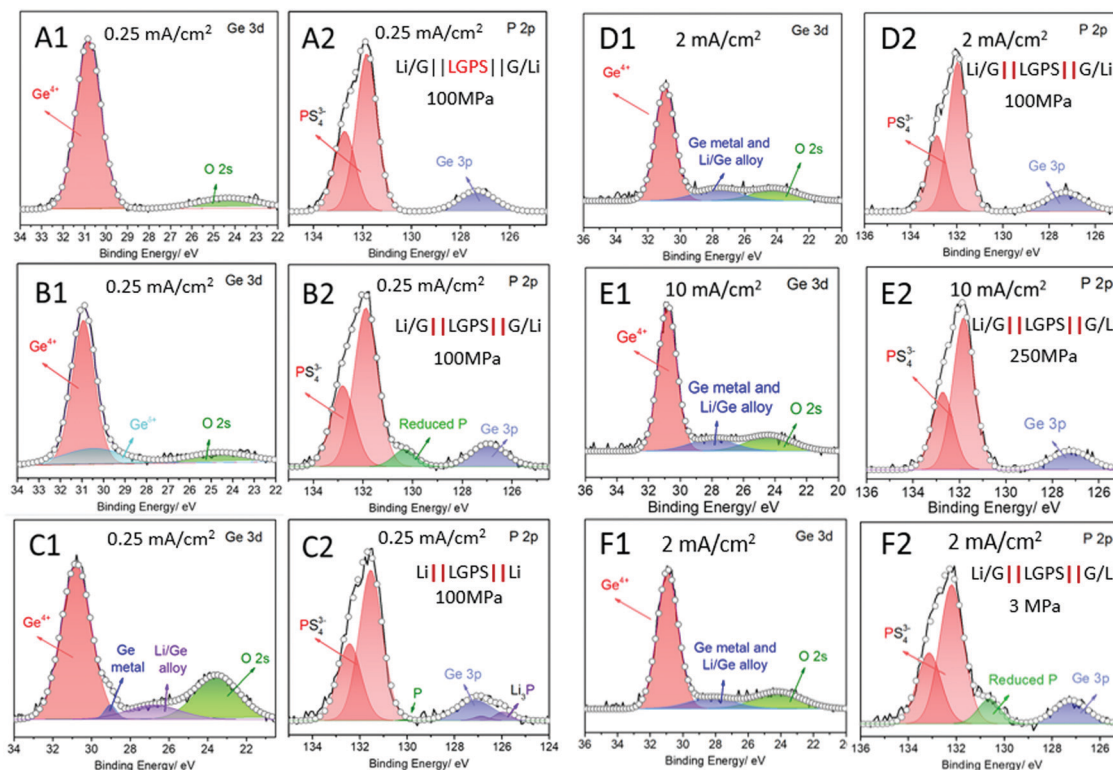


Fig. 5 XPS measurement of Ge and P for anode–LGPS–anode symmetric batteries with the X-ray beam focused on (A) the center part LGPS away from the interface with Li/G and (B) the interface between Li/G and LGPS in the Li/G–LGPS–G/Li cell under 100 MPa after 12 hours' cycling at 0.25 mA cm^{-2} ; (C) the interface between Li and LGPS in the Li–LGPS–Li symmetric battery under 100 MPa after 10 hours' cycling at 0.25 mA cm^{-2} (failed); (D) the Li/G–LGPS interface after the rate test at 2 mA cm^{-2} under 100 MPa and (E) 10 mA cm^{-2} under 250 MPa; and (F) the Li/G–LGPS interface at 2 mA cm^{-2} under 3 MPa.

state decomposition products of Fig. 4. However, at high currents, η' begins to dominate and favors metastable phases, such as Li_xGe_y at high K_{eff} , in our computations, which are not shown in Fig. 4 as they are all ground state phases in each voltage range.

The impedance profiles before and after CV tests (Fig. S9A, ESI[†]) under 100 MPa or 3 MPa are compared in Fig. S9B and C (ESI[†]) after fitting with the model shown in Fig. S9D (ESI[†]). The calculated R_{bulk} (bulk resistance) and R_{ct} (charge transfer resistance, here it is majorly the interface resistance) are listed in Table S2 (ESI[†]). R_{ct} (38.8Ω) under 100 MPa is much smaller than that under 3 MPa (395.4Ω) due to the better contact at high pressure. After the CV test, there is hardly any change of R_{bulk} for the battery under 100 MPa, while that of the battery under 3 MPa increases from 300Ω to 600Ω . The significantly elevated resistance is attributed to the more severe decomposition of LGPS under an ineffective mechanical constriction. Again, from electrochemical tests, it is proven that the degree of decomposition is significantly inhibited under optimum constriction conditions.

Conclusion

A lithium–graphite composite enables the application of a high external pressure during the testing of solid-state batteries with LGPS as the electrolyte. This creates a high mechanical constriction on the materials level that contributes to the excellent

rate performance of the Li/G–LGPS–G/Li symmetric battery. After cycling at high current densities up to 10 mA cm^{-2} for such solid-state batteries, cycling can still be performed normally at low rates, suggesting that there is no lithium dendrite penetration or short circuit. The reduction pathways of LGPS decomposition under different mechanical constrictions are analyzed by using both experimental XPS measurements and DFT computational simulations. It shows, for the first time, that under a proper mechanical constraint, the LGPS reduction follows a different pathway. This pathway, however, can be influenced kinetically by the high current density induced overpotential. Therefore, the decomposition of LGPS is a function of both mechanical constriction and current density. From the battery cycling performance and impedance tests, it is shown that high mechanical constriction along with the kinetically limited decomposition pathway reduces the total impedance and realizes a LGPS–lithium metal battery with excellent rate capability.

Methods

Electrochemistry

LGPS was either purchased from MSE Supplies or synthesized following previous methods.^{8,14,17} The graphite thin film is made by mixing the active materials with PTFE. The weight ratio of the graphite film is graphite:PTFE = 95:5. All the batteries are

assembled using a homemade pressurized cell in an argon-filled glovebox with oxygen and water <0.1 ppm. The symmetric battery (Li/G-LGPS-G/Li or Li-LGPS-Li) was made by pre-pressing three layers of Li/(graphite)-LGPS powder-(graphite)/Li together and keeping at different pressures during the battery tests. The Li foil and graphite film were rolled into a very thin layer with a thickness of around 30–35 μm and 25–30 μm , respectively. The weight of the lithium foil is around 1 mg with a diameter of 5/16'. The weight of the graphite film is 4–5 mg with a diameter of 3/8'. The weight and thickness of the LGPS pellet after pre-pressing are 100 mg and 500 μm . The thickness of Li-LGPS-Li, Li/G-LGPS-G/Li, G-LGPS-G and LGPS pellets under pressure was measured by a material testing machine (Fig. S10, ESI[†]). The batteries were charged and discharged at different current densities with a total capacity of 0.25 mA h cm⁻² for each cycle. LiCoO₂ half batteries were made by cold pressing a Li/graphite composite-LGPS powder-cathode film using a hydraulic press and keeping the pressure at 100–250 MPa. LiCoO₂ is coated with LiNbO₃ using the sol-gel method.¹⁴ The weight ratio of all the cathode films is active materials:LGPS:PTFE = 68:29:3. Battery cycling data were obtained on a LAND battery testing system. The average weight of the cathode film is around 3 mg. The specific capacity is calculated based on the weight of LCO in the cathode; the capacity ratio of the positive to negative electrodes (P/N ratio) is 0.57 based on the capacity of graphite and 0.16 based on the Li/G composite. The cyclic performance was tested at 0.1C at 25 °C. The CV test (Li/G-LGPS-LGPS/C) was conducted on a Solartron 1400 cell test system between OCV and 0.1 V with a scan rate of 0.1 mV s⁻¹. The LGPS cathode film for the CV test was made with LGPS:super P:PTFE = 87:10:3.

Material characterization

XRD. The XRD sample was prepared by hand-milling LGPS powder with lithium metal and/or graphite with a weight ratio = 1:1 in a glovebox. The powder mixtures were put on a hotplate and heated to the nominal temperature (500 °C) for 36 hours and then characterized by XRD. XRD data were obtained using a Rigaku Miniflex 6G. The mixtures of LGPS and graphite before and after the high temperature treatment were sealed with Kapton film in an argon-filled glovebox to prevent the air contamination.

SEM and XPS. Cross-section imaging of the pellet of Li/graphite-LGPS-graphite/Li was performed using a Supra 55 SEM. The pellet was broken into small pieces and attached onto the side of a screw nut with carbon tape to make it perpendicular to the electron (or X-ray) beam. The screw nuts with the samples were mounted onto a standard SEM stub and sealed into two plastic bags inside an argon-filled glove box. FIB-SEM imaging was conducted on an FEIHelios 660 dual-beam system. XPS was performed using a Thermo Scientific K-Alpha+ with a beam size of 70 μm . The samples were mounted onto a standard XPS sample holder and sealed with plastic bags as well. All samples were transferred into a vacuum environment in about 10 seconds. All XPS results were fitted through peak-differentiating and imitating *via* Avantage.

Computational methods. All DFT calculations were performed using the Vienna Ab initio Simulation Package (VASP)

following the Materials Project calculation parameters.⁴² A *K*-point density of 1000 kppa, a cutoff of 520 eV, and the VASP recommended pseudopotentials were used. Mechanically constrained phase diagrams were calculated using Lagrange minimization schemes as outlined in ref. 14 for effective moduli of 0, 5, 10 and 15 GPa. All Li-Ge-P-S phases in the Materials Project database were considered. Bader charge analysis and spin polarized calculations were used to determine the charge valence.

Conflicts of interest

The authors declare no conflict of interest.

Acknowledgements

The work is supported by Dean's competitive fund for promising scholarship at Harvard University and the GIC (Global Innovation Contest) fund of LG Chem, Ltd. Y. S. is thankful for the support from Chinese Scholarship Council (CSC) and the home institution of Tsinghua University as a visiting graduate student at Harvard University for one year. L. Y. thanks Baohong Chen for measuring the loaded thickness of the pellets. The XPS, SEM and FIB-SEM experiments were conducted at the Center for Nanoscale Systems (CNS) at Harvard University, supported by the National Science Foundation. X. L. conceived the project and supervised all aspects of the research. Y. S., L. Y., E. G., and I. K. conducted the electrochemical tests, sample preparation, and SEM characterization. Y. S. and Y. W. performed the XPS characterization. W. F. and Y. W. performed the DFT simulation. Y. S., L. Y., W. F. and X. L. analyzed the results and wrote the manuscript.

References

- 1 J. Janek and W. G. Zeier, A solid future for battery development, *Nat. Energy*, 2016, **1**, 1–4.
- 2 J. Liu, *et al.*, Pathways for practical high-energy long-cycling lithium metal batteries, *Nat. Energy*, 2019, **4**, 180–186.
- 3 A. Manthiram, X. Yu and S. Wang, Lithium battery chemistries enabled, *Nat. Rev. Mater.*, 2017, **2**, 1–16.
- 4 X. Chen, W. He, L. X. Ding, S. Wang and H. Wang, Enhancing interfacial contact in all solid state batteries with a cathode-supported solid electrolyte membrane framework, *Energy Environ. Sci.*, 2019, **12**, 938–944.
- 5 Y. Kato, *et al.*, High-power all-solid-state batteries using sulfide superionic conductors, *Nat. Energy*, 2016, **1**, 16030.
- 6 N. Kamaya, *et al.*, A lithium superionic conductor, *Nat. Mater.*, 2011, **10**, 682–686.
- 7 F. Wu, W. Fitzhugh, L. Ye, J. Ning and X. Li, Advanced sulfide solid electrolyte by core-shell structural design, *Nat. Commun.*, 2018, **9**, 1–11.
- 8 S. Wenzel, *et al.*, Direct Observation of the Interfacial Instability of the Fast Ionic Conductor Li₁₀GeP₂S₁₂ at the Lithium Metal Anode, *Chem. Mater.*, 2016, **28**, 2400–2407.

- 9 Y. Zhu, X. He and Y. Mo, First principles study on electrochemical and chemical stability of solid electrolyte-electrode interfaces in all-solid-state Li-ion batteries, *J. Mater. Chem. A*, 2016, **4**, 3253–3266.
- 10 S. P. Ong, *et al.*, Phase stability, electrochemical stability and ionic conductivity of the $\text{Li}_{10} \pm 1\text{MP}_2\text{X}_{12}$ (M = Ge, Si, Sn, Al or P, and X = O, S or Se) family of superionic conductors, *Energy Environ. Sci.*, 2013, **6**, 148–156.
- 11 F. Han, Y. Zhu, X. He, Y. Mo and C. Wang, Electrochemical Stability of $\text{Li}_{10}\text{GeP}_2\text{S}_{12}$ and $\text{Li}_7\text{La}_3\text{Zr}_2\text{O}_{12}$ Solid Electrolytes, *Adv. Energy Mater.*, 2016, **6**, 1501590.
- 12 P. Bron, B. Roling and S. Dehnen, Impedance characterization reveals mixed conducting interphases between sulfidic superionic conductors and lithium metal electrodes, *J. Power Sources*, 2017, **352**, 127–134.
- 13 W. Fitzhugh, *et al.*, A High-Throughput Search for Functionally Stable Interfaces in Sulfide Solid-State Lithium Ion Conductors, *Adv. Energy Mater.*, 2019, **9**, 1–12.
- 14 W. Fitzhugh, F. Wu, L. Ye, H. Su and X. Li, Strain-Stabilized Ceramic-Sulfide Electrolytes, *Small*, 2019, **1901470**, 1–14.
- 15 W. Fitzhugh, L. Ye and X. Li, The effects of mechanical constriction on the operation of sulfide based solid-state batteries, *J. Mater. Chem. A*, 2019, **7**, 23604–23627.
- 16 R. Koerver, *et al.*, Chemo-mechanical expansion of lithium electrode materials-on the route to mechanically optimized all-solid-state batteries, *Energy Environ. Sci.*, 2018, **11**, 2142–2158.
- 17 N. Kamaya, *et al.*, A lithium superionic conductor, *Nat. Mater.*, 2011, **10**, 682–686.
- 18 K. Yoon, J. J. Kim, W. M. Seong, M. H. Lee and K. Kang, Investigation on the interface between $\text{Li}_{10}\text{GeP}_2\text{S}_{12}$ electrolyte and carbon conductive agents in all-solid-state lithium battery, *Sci. Rep.*, 2018, **8**, 1–7.
- 19 F. Han, *et al.*, High electronic conductivity as the origin of lithium dendrite formation within solid electrolytes, *Nat. Energy*, 2019, **4**, 187–196.
- 20 J. Kasemchainan, *et al.*, Critical stripping current leads to dendrite formation on plating in lithium anode solid electrolyte cells, *Nat. Mater.*, 2019, **18**, 1105–1111.
- 21 T. Swamy, *et al.*, Lithium metal penetration induced by electrodeposition through solid electrolytes: example in single-crystal $\text{Li}_6\text{La}_3\text{ZrTaO}_{12}$ garnet, *J. Electrochem. Soc.*, 2018, **165**, A3648–A3655.
- 22 L. Porz, *et al.*, Mechanism of Lithium Metal Penetration through Inorganic Solid Electrolytes, *Adv. Energy Mater.*, 2017, **7**, 1–12.
- 23 P. Adeli, *et al.*, Boosting Solid-State Diffusivity and Conductivity in Lithium Superionic Argvrodites by Halide Substitution, *Angew. Chem., Int. Ed.*, 2019, **58**, 8681–8686.
- 24 S. Wenzel, S. J. Sedlmaier, C. Dietrich, W. G. Zeier and J. Janek, Interfacial reactivity and interphase growth of argyrodite solid electrolytes at lithium metal electrodes, *Solid State Ionics*, 2018, **318**, 102–112.
- 25 R. Koerver, *et al.*, Chemo-mechanical expansion of lithium electrode materials-on the route to mechanically optimized all-solid-state batteries, *Energy Environ. Sci.*, 2018, **11**, 2142–2158.
- 26 T. Krauskopf, H. Hartmann, W. G. Zeier and J. Janek, Toward a Fundamental Understanding of the Lithium Metal Anode in Solid-State Batteries – An Electrochemo-Mechanical Study on the Garnet-Type Solid Electrolyte $\text{Li}_{6.25}\text{Al}_{0.25}\text{La}_3\text{Zr}_2\text{O}_{12}$, *ACS Appl. Mater. Interfaces*, 2019, **11**, 14463–14477.
- 27 R. H. Basappa, T. Ito and H. Yamada, Contact between garnet-type solid electrolyte and lithium metal anode: influence on charge transfer resistance and short circuit prevention, *J. Electrochem. Soc.*, 2017, **164**, A666–A671.
- 28 H. Koshikawa, *et al.*, Dynamic changes in charge-transfer resistance at Li metal/ $\text{Li}_7\text{La}_3\text{Zr}_2\text{O}_{12}$ interfaces during electrochemical Li dissolution/deposition cycles, *J. Power Sources*, 2018, **376**, 147–151.
- 29 A. Shellikeri, *et al.*, Investigation of pre-lithiation in graphite and hard-carbon anodes using different lithium source structures, *J. Electrochem. Soc.*, 2017, **164**, A3914–A3924.
- 30 H. J. Guo, *et al.*, Diffusion coefficient of lithium in artificial graphite, mesocarbon microbeads, and disordered carbon, *New Carbon Mater.*, 2007, **22**, 7–10.
- 31 D. Di Stefano, *et al.*, Superionic Diffusion through Frustrated Energy Landscape, *Chem*, 2019, **5**, 2450–2460.
- 32 A. J. Bard and L. R. Faulkner, Fundamentals and applications, *Electrochem. Methods*, 2001, **2**, 307–312.
- 33 Y. Zhu, X. He and Y. Mo, Origin of Outstanding Stability in the Lithium Solid Electrolyte Materials: Insights from Thermodynamic Analyses Based on First-Principles Calculations, *ACS Appl. Mater. Interfaces*, 2015, **7**, 23685–23693.
- 34 P. C. Donohue and H. S. Young, Synthesis, structure, and superconductivity of new high pressure phases in the systems GeP and GeAs, *J. Solid State Chem.*, 1970, **1**, 143–149.
- 35 W. Fitzhugh, L. Ye and X. Li, The effects of mechanical constriction on the operation of sulfide based solid-state batteries, *J. Mater. Chem. A*, 2019, **7**, 23604–23627.
- 36 C. Wang, *et al.*, Manipulating Interfacial Nanostructure to Achieve High-Performance All-Solid-State Lithium-Ion Batteries, *Small Methods*, 2019, 1900261, DOI: 10.1002/smt.201900261.
- 37 F. Han, T. Gao, Y. Zhu, K. J. Gaskell and C. Wang, A battery made from a single material, *Adv. Mater.*, 2015, **27**, 3473–3483.
- 38 K. Prabhakaran and T. Ogino, Oxidation of Ge(100) and Ge(111) surfaces: an UPS and XPS study, *Surf. Sci.*, 1995, **325**, 263–271.
- 39 H. G. Von Schnering and W. Hönlle, Bridging Chasms with Polyphosphides, *Chem. Rev.*, 1988, **88**, 243–273.
- 40 S. Wenzel, *et al.*, Interphase formation and degradation of charge transfer kinetics between a lithium metal anode and highly crystalline $\text{Li}_7\text{P}_3\text{S}_{11}$ solid electrolyte, *Solid State Ionics*, 2016, **286**, 24–33.
- 41 W. Fitzhugh and X. Li, Modulation of Ionic Current Limitations by Doping Graphite Anodes, *J. Electrochem. Soc.*, 2018, **165**, 2233–2238.
- 42 A. Jain, *et al.*, Commentary: The materials project: a materials genome approach to accelerating materials innovation, *APL Mater.*, 2013, **1**, 011002.